Non-contact rheology of finite-size air-water interfaces

Vincent Bertin, Zaicheng Zhang, Rodolphe Boisgard, Christine Grauby-Heywang, Elie Raphael, Thomas Salez, Abdelhamid Maali

Non-contact rheology of finite-size air-water interfaces

Vincent Bertin,[1,2,*] Zaicheng Zhang,[1,*] Rodolphe Boisgard,[1] Christine Grauby-Heywang,[1] Elie Raphaël,[2] Thomas Salez,[1,3,†] and Abdelhamid Maali[1,‡]

[1] *Univ. Bordeaux, CNRS, LOMA, UMR 5798, 33405 Talence, France.*
[2] *UMR CNRS Gulliver 7083, ESPCI Paris, PSL Research University, 75005 Paris, France.*
[3] *Global Station for Soft Matter, Global Institution for Collaborative Research and Education, Hokkaido University, Sapporo, Hokkaido 060-0808, Japan.*

(Dated: November 6, 2020)

We present non-contact atomic-force microscopy measurements of the hydrodynamic interactions between a rigid sphere and an air bubble in water at the micro-scale. The size of the bubble is found to have a significant effect on the response due to the long-range capillary deformation of the air-liquid interface. To rationalize the experimental data, we develop a viscocapillary lubrication model accounting for the finite-size effect. The comparison between experiments and theory allows us to measure the air-liquid surface tension, without contact, paving the way towards robust non-contact tensiometry of polluted air-liquid interfaces.

The interface between two media has an energy cost per unit surface, called surface tension, resulting from the microscopic interactions of the constitutive molecules at the interface [1, 2]. Surface tension is an important parameter in soft condensed matter and at small scales where capillary phenomena usually dominate. Examples include wetting properties [3, 4], thin-film dynamics [5, 6], multiphase flows...

Surface active molecules – *i.e.* surfactants – are widely used to stabilize capillary interfaces on purpose, *e.g.* in emulsions or foams, but are also inevitable due to pollution. These contaminants, which are usually adsorbed at the interface between two immiscible fluids, lower the surface tension and are responsible for specific rheological properties of the interface [7]. To understand the dynamics of soft materials, the interaction between objects such as droplets and bubbles, or to quantify the amount of interfacial contamination, capillary interfacial rheology is essential. Specifically, surface tension is measured by a large variety of techniques: pendant-drop method [8], spinning-drop method, Wilhelmy plates or du Noüy rings [9], for instance. Moreover, the interfacial rheology is usually measured with the Langmuir trough [10] or through oscillating-disk devices [11].

A complementary device to measure material properties is atomic-force microscope (AFM), which has recently been used to study capillary phenomena such as the interaction between bubbles [12, 13] or droplets [14–16], the hydrodynamic boundary condition at a water-air interface [17, 18], and dynamical wetting [19–24]. Recently, the AFM has also been employed in a dynamical mode, and appears to be a remarkable tool to quantify properties – with the advantage of providing non-contact measurements [25–29].

In this Letter, we study the force exerted on a water-immersed sphere attached to an AFM cantilever, that is driven to oscillate near the apex of an air bubble. The deformation of the bubble and the force exerted on the spherical probe are coupled, and result from the hydrodynamic pressure induced by the oscillating water flow. To rationalize the experimental data, we develop a lubrication model accounting for finite-size effects – which are found to be significant in the linear viscocapillary response. All together, this method allows for robust interfacial rheology in the absence of any direct contact.

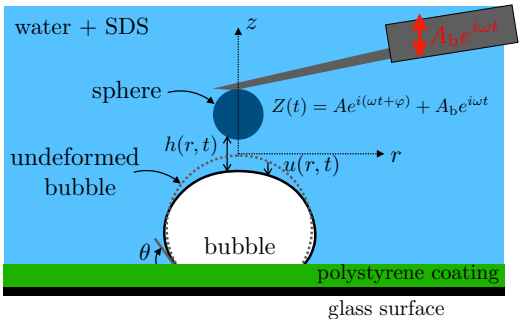

Figure 1: A spherical probe (dark blue) attached to an AFM cantilever (grey) oscillates vertically, along the z axis, within a water-Sodium Dodecyl Sulfate (SDS) liquid solution (light blue) and near an air bubble (white). The motion results in an axisymmetric liquid-gap thickness profile $h(r,t)$ depending on the radial distance r and time t, that includes an axisymmetric vertical deformation field $u(r,t)$ of the bubble surface along the $-z$ direction, with respect to its equilibrium spherical-cap shape (dashed line).

A schematic of the experimental setup in shown in Fig. 1 [18, 30]. The cantilever is excited by the base oscillation $\mathcal{R}[A_b e^{i\omega t}]$, where ω and A_b are the angular frequency and amplitude of the base vibration, respectively, and $\mathcal{R}[.]$ denotes the real part. The system essentially behaves as a damped oscillator, where the vertical displacement $Z(t)$ of the center of mass of the sphere with respect to its rest position satisfies:

$$m_c \ddot{Z} + \Gamma_{\rm bulk} \dot{Z} + k_c Z = F_d + F \ , \qquad (1)$$

with m_c the effective mass (*i.e.* including the added fluid mass) in the bulk, Γ_{bulk} the damping coefficient in the bulk, k_c the stiffness of the cantilever, F_d the driving force due to the imposed oscillation of the cantilever, and $F = \mathcal{R}[F^* e^{i\omega t}]$ the hydrodynamic force resulting from the interaction between the oscillating sphere and the air-liquid interface. The displacement $Z(t)$ of the sphere includes the cantilever deflection $\mathcal{R}[Ae^{i(\omega t+\varphi)}]$ measured by AFM and the base displacement, and thus reads $Z(t) = \mathcal{R}[Ae^{i(\omega t+\varphi)} + A_b e^{i\omega t}] = \mathcal{R}[Z^* e^{i\omega t}]$, where A and $Z^* = Ae^{i\varphi} + A_b$ are real and complex amplitudes respectively [30]. We further define the mechanical impedance $G^* = -F^*/Z^*$. Invoking the complex version of Eq. (1), the impedance reads:

$$G^* = -k_c \left[1 - \left(\frac{\omega}{\omega_0}\right)^2 + i\frac{\omega}{\omega_0 Q}\right] \frac{Ae^{i\varphi} - A_\infty e^{i\varphi_\infty}}{Ae^{i\varphi} + A_b} \ , \quad (2)$$

where A_∞ and φ_∞ are respectively the amplitude (A) and phase (φ) measured far from the bubble (*i.e.* where F vanishes), $\omega_0 = \sqrt{k_c/m_c}$ is the bulk resonance frequency, and $Q = m_c\omega_0/\Gamma_{bulk}$ is the bulk quality factor. Equation (2) provides a direct way to measure G^* experimentally from the cantilever's deflection signal.

To model theoretically G^*, we consider the axisymmetric system composed of the rigid sphere located at an average distance D from the apex of the undeformed air bubble. The ensemble is immersed in an incompressible Newtonian fluid with a dynamical shear viscosity η. The liquid-gap thickness is approximated by the near-axis parabolic expansion:

$$h(r,t) \simeq D + \frac{r^2}{2R_{eff}} + Z(t) + u(r,t) \ , \quad (3)$$

with $R_{eff}^{-1} = R_s^{-1} + R_b^{-1}$, and where R_s and R_b are the curvature radii of the sphere and bubble, respectively. We focus on the situation where $D \ll R_{eff}$, so that we can invoke the lubrication approximation of the steady Stokes equations. The experiments are done at low enough frequencies so that we can assume a no-slip boundary condition at the air-liquid interface [18]. Such a condition is also assumed at the sphere-liquid interface. Therefore, the liquid-gap thickness obeys the Reynolds equation [31]:

$$\frac{\partial h(r,t)}{\partial t} = \frac{1}{12\eta r}\frac{\partial}{\partial r}\left[r h(r,t)^3 \frac{\partial}{\partial r} p(r,t)\right] \ , \quad (4)$$

where $p(r,t)$ is the excess hydrodynamic pressure field with respect to the rest state. Since, in the lubrication approximation, the excess pressure is invariant along z, it can be evaluated at the air-liquid interface through the linearized Young-Laplace equation [15]:

$$p(r,t) \simeq \gamma \frac{1}{r}\frac{\partial}{\partial r}\left[r\frac{\partial u(r,t)}{\partial r}\right] \ , \quad (5)$$

where γ denotes the air-liquid surface tension, and where small slopes are assumed. The contribution of Hamaker forces is neglected in the model, as the sphere-bubble distance in the experiment is in the 10 nm - 20 μm range, and thus typically larger than the distance below which these forces are dominant. We further assume a small amplitude of the sphere's oscillation, so that we can invoke the linear-response framework, and thus write: $u(r,t) = \mathcal{R}[u^*(r)e^{i\omega t}]$ and $p(r,t) = \mathcal{R}[p^*(r)e^{i\omega t}]$, with $u^*(r)$ and $p^*(r)$ the corresponding complex amplitudes. Such a viscocapillary problem is sensitive to the total size of the system, as in Refs. [15, 32] where it has been shown that the central deformation diverges logarithmically with the system size. Therefore, it is appropriate to introduce a cut-off radius b, beyond which we enforce $p^*(r > b) = 0$ and $u^*(r > b) = 0$. Finally, the amplitude of the hydrodynamic force reads $F^* = 2\pi \int_0^b \mathrm{d}r\, r\, p^*(r)$ in the lubrication approximation, which allows us to compute the mechanical impedance G^* [33].

The experiments are performed using an AFM (Bioscope, Bruker) equipped with a liquid cell (DTFML-DD-HE). A spherical borosilicate particle (MO-Sci Corporation) with a $R_s = 54 \pm 2$ μm radius is glued at the edge of a silicon nitride cantilever (ORC8-10, Bruker AFM Probes). The stiffness $k_c = 0.20 \pm 0.01$ N/m of the cantilever (with the sphere attached to it) is determined from the drainage method [34]. The bulk resonance frequency $\omega_0/(2\pi) = 1240 \pm 3$ Hz and the bulk quality factor $Q = 3.4 \pm 0.1$ are obtained from the resonance spectrum at large distance [30]. Air microbubbles are deposited onto spincoated polystyrene layers, within Sodium Dodecyl Sulfate (SDS) solutions in water. The SDS concentrations C are in the $0.2 - 40.0$ mM range. As measured with an optical microscope, the bubble radii R_b are in the $0.200 - 0.6$ mm range, and the contact angles θ (see definition in Fig. 1) are in the $40 - 90°$ range, with the exact value depending on C. A multi-axis piezo stage (NanoT series, Mad City Labs) is used to control the distance between the sphere and the bubble, by imposing a displacement to the substrate at very low velocity. The amplitude A and phase φ of the cantilever's deflection signal are measured by a lock-in amplifier (Model 7280, Signal Recovery), and are recorded versus the piezo displacement. Additionally, the DC component of the cantilever's deflection is also recorded and used to determine the average gap distance D.

The real and imaginary parts of the measured mechanical impedance $G^* = G' + iG''$ are plotted in Fig. 2 as functions of the average sphere-bubble distance D, for two frequencies. Best fits to the model [33] are also shown, in good agreement with the data, with the air-

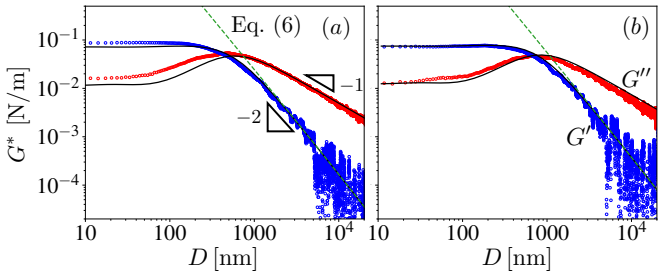

Figure 2: Real (blue circles) and imaginary (red circles) parts of the measured mechanical impedance $G^* = G' + iG''$ versus average sphere-bubble distance D, for a surfactant $C = 1\,\mathrm{mM}$, and frequencies $\omega/(2\pi) = 200$ Hz (a), and 300 Hz (b). The bubble radius is $R_\mathrm{b} = 346 \pm 2$ μm and the contact angle is $\theta = 81 \pm 2°$. The best fits to the model [33] are displayed with solid black lines, using a single fitting parameter $\gamma = 58 \pm 4$ mN/m. The large-distance asymptotic solution for G' (see Eq. (6)) is also shown with green dashed lines. The slope triangles indicate power-law exponents.

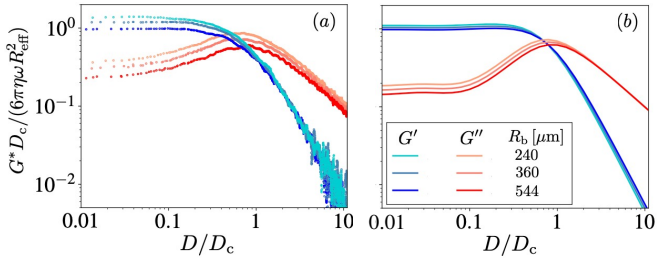

Figure 3: Dimensionless mechanical impedance versus dimensionless distance, for three bubble sizes as indicated, a single frequency $\omega/(2\pi) = 200$ Hz, and a single surfactant concentration $C = 1\,\mathrm{mM}$. The experimental data are show in (a). The results of the model are plotted in (b), using the previously-obtained best-fit parameter $\gamma = 58$ mN/m, and the cut-off radius $b = (\pi - \theta)R_\mathrm{b}$ with $\theta = 81°$.

liquid surface tension $\gamma = 58 \pm 4$ mN/m as the only fitting parameter. We note that we used half the contour length of the undeformed air-liquid interface as a cut-off radius in the model, *i.e.* $b = (\pi - \theta)\, R_\mathrm{b}$.

Furthermore, two asymptotic regimes can be observed, at large and small distance respectively. They crossover near $D \approx 1000\,\mathrm{nm}$, which corresponds to the typical viscocapillary distance $D_\mathrm{c} = 16R_\mathrm{eff}^2\eta\omega/\gamma$ emerging from the model [33], and equal to 727 and 1091 nm in Figs. 2(a) and (b), respectively. At large distance, the viscous contribution G'' dominates and follows a $\sim D^{-1}$ scaling law, as expected from the asymptotic expression $G'' \simeq 6\pi\eta R_\mathrm{eff}^2\omega/D$ [25]. In contrast, the restoring contribution G' due to the air-liquid capillary interface appears with an apparent $\sim D^{-2}$ scaling law at large distance. We stress that the latter is not an exact scaling law, due to a logarithmic correction [33]:

$$G'(D) \simeq \frac{9\pi\eta^2 R_\mathrm{eff}^3\omega^2}{\gamma D^2}\left[-1 + \log\left(1 + \frac{b^2}{2R_\mathrm{eff}D}\right)\right]. \quad (6)$$

At small distance, both G' and G'' saturate to constant values, which is reminiscent of elastohydrodynamic responses near soft substrates [25–27, 29, 35, 36], and might be related to saturations in the deformation and pressure fields. At such small distances, the capillary deformation of the bubble surface essentially accommodates the sphere's oscillation, and the liquid is no longer expelled from the gap, which further leads to a stronger capillary response than the viscous one.

In order to reveal the importance of finite-size effects in the viscocapillary response, we introduce the dimensionless mechanical impedance $\mathcal{G}^* = G^* D_\mathrm{c}/(6\pi\eta\omega R_\mathrm{eff}^2)$. In Fig. 3, the experimental and theoretical dimensionless mechanical impedances are plotted versus the dimensionless average sphere-bubble distance, for three bubble radii. Except for the viscous contribution in the large-distance limit, the dimensionless impedance is generally found to depend on the bubble size in a nontrivial way, which is correctly reproduced by the model. This observation highlights the importance of finite-size effects in viscocapillary contacts. We note that the logarithmic correction in the large-distance asymptotic expression of the capillary contribution (see Eq. (6)) contains a bubble-size dependence which cannot be resolved with the AFM sensitivity and the current bubble-size range. At small distance, the size dependence is more pronounced and both the real and imaginary parts of the dimensionless impedance decrease when increasing the bubble size.

Having discussed the finite-size effects on the global hydrodynamic force, we now investigate their influence on the amplitudes of the local excess pressure and deformation fields. Figure 4 shows the results from the model [33] for $D/D_\mathrm{c} = 10$, with the same parameters as in Fig. 3. We observe that both the real and imaginary parts of the amplitude of the dimensionless excess pressure field decay rapidly, on a typical distance $\sim \sqrt{R_\mathrm{eff}D}$. The imaginary part does itself not depend on the cut-off radius, and is well described by the leading-order rigid-like result (see Eq. (S16)) in the large-distance asymptotic model [33]. Besides, the real part depends weakly on the cut-off radius, through the dimensionless number $b/\sqrt{2R_\mathrm{eff}D}$, as predicted by the next-order correction (see Eq. (S18)) in the large-distance asymptotic model [33]. This dependence in the cut-off radius yields the logarithmic correction in Eq. (6). In contrast, both the real and imaginary parts of the amplitude of the dimensionless deformation field depend notably on the cut-off radius. This fact results from the long-range capillary deformation of the air-liquid interface, and explains the significant finite-size effects in our global viscocapillary measurements.

So far, the air-liquid surface tension was considered as a free parameter and was fixed by fitting the AFM experimental data to the model. The fitted values of the

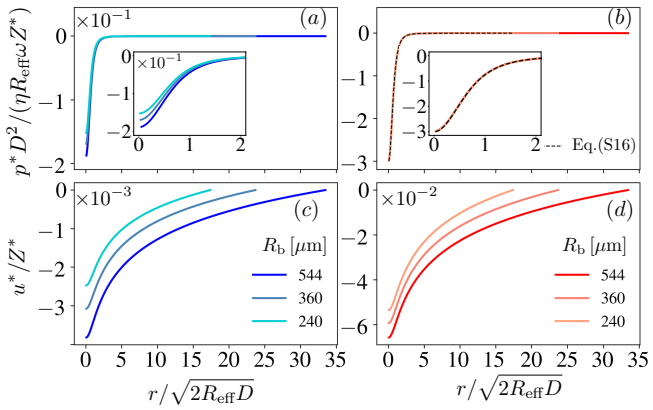

Figure 4: Real (a) and imaginary (b) parts of the amplitude of the dimensionless excess pressure field as functions of the dimensionless radial coordinate, at a dimensionless distance $D/D_c = 10$, for the three bubble radii of Fig. 3, as obtained from the model [33]. The insets display zooms near the symmetry axis. In panel (b), Eq. (S16) [33] is plotted (dashed line) for comparison. Similarly, the real and imaginary parts of the amplitude of the dimensionless deformation field are plotted in panels (c) and (d), respectively.

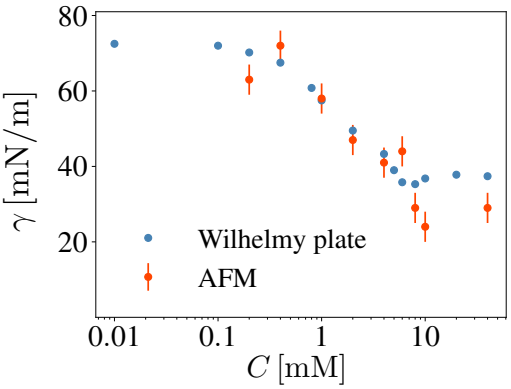

Figure 5: Air-water surface tension as a function of surfactant (SDS) concentration, as obtained from fits (see Fig. 2) of the AFM experimental data by the model (red dots). For comparison, independent measurements using the Wilhelmy-plate method are provided (blue dots).

surface tension as a function of the SDS concentration in water are shown in Fig. 5. We observe that the surface tension globally decreases with increasing surfactant concentration, as expected. At surfactant concentrations smaller than $\sim$ 0.5 mM, the surface tension is close to the 72 mN/m value for pure water. At concentrations larger than $\sim$ 8 mM, the surface tension saturates to a value on the order of 30 mN/m. The critical micellar concentration of SDS in water is estimated to be around 8 mM [37, 38], which is in agreement with the latter observation. The uncertainty on the fitted surface tension is on the order of $\pm$4 mN/m and may result from two main sources: i) the experiments at different frequencies lead to fitted values which vary by a few percents; ii) we take half the contour length of the undeformed air-liquid interface as an arbitrary cut-off radius, while one could possibly make other choices, *e.g.* the curvature radius of the undeformed interface, which would modify slightly the fitted values.

Finally, we discuss the capacity of our method to be used as a robust tensiometer. To do so, we performed independent tensiometry experiments on similar air-water-SDS interfaces using the Wilhelmy-plate method [9]. The results are shown in Fig. 5, and agree well with the ones obtained with our method. Possible systematic deviations at the highest concentrations may result from a surfactant-induced depinning of the contact line of the bubble on the substrate [39]. In such a scenario, the hydrodynamic pressure would not only trigger a local capillary deformation (see Eq. (5)), but would also induce a spreading-dewetting cycle of the bubble on the substrate. In addition, the bubble resonance frequency being lower at lower surface tension, capillary waves might be excited at the air-liquid interface at large surfactant concentrations.

In conclusion, we have studied the viscocapillary interaction between an air bubble and a spherical probe attached to an AFM cantilever, and immersed within a surfactant solution in water. The sphere was oscillated in the direction normal to the air-liquid interface, thus generating a flow and an associated hydrodynamic pressure field that could deform the interface. The resulting force exerted on the sphere was measured as a function of the sphere-bubble distance, and found to depend on the bubble size. We also developed a model, coupling axisymmetric lubrication flow and capillary deformations, and accounting for finite-size effects through a cut-off radial distance. The experimental results were found to be in good agreement with the model, when assuming the cut-off radius to be half the contour length of the undeformed air-liquid interface, and with the air-liquid surface tension as a single free parameter. Finally, from a comparison with independent tensiometry measurements using the Wilhelmy-plate method, we discussed the capacity of our novel method to measure surface tensions robustly. The volume of the liquid required in our method can be as small as tens of microliters. All together, this work paves the way to non-contact capillary rheology, with fundamental perspectives in confined soft matter, and practical applications towards micro-monitoring of water contamination.

ACKNOWLEDGEMENTS

The authors thank Elisabeth Charlaix for preliminary discussions, as well as Samir Almohamad for technical assistance on the Wilhelmy-plate calibration experiments.

Z. Z. acknowledges financial support from the China Scholarship Council. Z. Z. and A. M. acknowledge financial support from Agence Nationale de la Recherche (ANR-19-CE30-0012).

* These authors contributed equally.
† Electronic address: thomas.salez@u-bordeaux.fr
‡ Electronic address: abdelhamid.maali@u-bordeaux.fr

[1] P.-G. De Gennes, F. Brochard-Wyart, and D. Quéré, Capillarity and wetting phenomena: drops, bubbles, pearls, waves (Springer Science & Business Media, 2013).
[2] A. Marchand, J. H. Weijs, J. H. Snoeijer, and B. Andreotti, American Journal of Physics **79**, 999 (2011).
[3] P.-G. De Gennes, Reviews of modern physics **57**, 827 (1985).
[4] D. Bonn, J. Eggers, J. Indekeu, J. Meunier, and E. Rolley, Reviews of modern physics **81**, 739 (2009).
[5] A. Oron, S. H. Davis, and S. G. Bankoff, Reviews of modern physics **69**, 931 (1997).
[6] R. V. Craster and O. K. Matar, Reviews of modern physics **81**, 1131 (2009).
[7] D. Langevin, Annual review of fluid mechanics **46**, 47 (2014).
[8] J. D. Berry, M. J. Neeson, R. R. Dagastine, D. Y. Chan, and R. F. Tabor, Journal of colloid and interface science **454**, 226 (2015).
[9] J. Drelich, C. Fang, and C. White, Encyclopedia of surface and colloid science **3**, 3158 (2002).
[10] D. K. Schwartz, C. M. Knobler, and R. Bruinsma, Physical review letters **73**, 2841 (1994).
[11] P. Erni, P. Fischer, E. J. Windhab, V. Kusnezov, H. Stettin, and J. Läuger, Review of scientific instruments **74**, 4916 (2003).
[12] I. U. Vakarelski, J. Lee, R. R. Dagastine, D. Y. Chan, G. W. Stevens, and F. Grieser, Langmuir **24**, 603 (2008).
[13] I. U. Vakarelski, R. Manica, X. Tang, S. J. O'Shea, G. W. Stevens, F. Grieser, R. R. Dagastine, and D. Y. Chan, Proceedings of the National Academy of Sciences **107**, 11177 (2010).
[14] R. R. Dagastine, R. Manica, S. L. Carnie, D. Chan, G. W. Stevens, and F. Grieser, Science **313**, 210 (2006).
[15] D. Y. Chan, E. Klaseboer, and R. Manica, Soft Matter **7**, 2235 (2011).
[16] R. F. Tabor, F. Grieser, R. R. Dagastine, and D. Y. Chan, Journal of colloid and interface science **371**, 1 (2012).
[17] O. Manor, I. U. Vakarelski, G. W. Stevens, F. Grieser, R. R. Dagastine, and D. Y. Chan, Langmuir **24**, 11533 (2008).
[18] A. Maali, R. Boisgard, H. Chraibi, Z. Zhang, H. Kellay, and A. Würger, Physical Review Letters **118**, 084501 (2017).
[19] S. Ecke, M. Preuss, and H.-J. Butt, Journal of adhesion science and technology **13**, 1181 (1999).
[20] X. Xiong, S. Guo, Z. Xu, P. Sheng, and P. Tong, Physical Review E **80**, 061604 (2009).
[21] M. Delmas, M. Monthioux, and T. Ondarçuhu, Physical review letters **106**, 136102 (2011).
[22] S. Guo, M. Gao, X. Xiong, Y. J. Wang, X. Wang, P. Sheng, and P. Tong, Physical review letters **111**, 026101 (2013).
[23] J. Dupré de Baubigny, M. Benzaquen, L. Fabié, M. Delmas, J.-P. Aimé, M. Legros, and T. Ondarçuhu, Langmuir **31**, 9790 (2015).
[24] C. Mortagne, K. Lippera, P. Tordjeman, M. Benzaquen, and T. Ondarçuhu, Physical Review Fluids **2**, 102201 (2017).
[25] S. Leroy and E. Charlaix, Journal of Fluid Mechanics **674**, 389 (2011).
[26] S. Leroy, A. Steinberger, C. Cottin-Bizonne, F. Restagno, L. Léger, and É. Charlaix, Physical Review Letters **108**, 264501 (2012).
[27] R. Villey, E. Martinot, C. Cottin-Bizonne, M. Phaner-Goutorbe, L. Léger, F. Restagno, and E. Charlaix, Physical Review Letters **111**, 215701 (2013).
[28] D. Guan, C. Barraud, E. Charlaix, and P. Tong, Langmuir **33**, 1385 (2017).
[29] Z. Zhang, V. Bertin, M. Arshad, E. Raphaël, T. Salez, and A. Maali, Phys. Rev. Lett. **124**, 054502 (2020).
[30] A. Maali and R. Boisgard, Journal of Applied Physics **114**, 144302 (2013).
[31] O. Reynolds, Philos. Trans. R. Soc. Lond. **177**, 157 (1886).
[32] Y. Wang, B. Zeng, H. T. Alem, Z. Zhang, E. Charlaix, and A. Maali, Langmuir **34**, 1371 (2018).
[33] Supplementary Material can be found at [link to be added by the editors]. The document provides further technical details on the computation of the mechanical impedance, and its asymptotic analytical expression at large distances. (2000).
[34] V. S. Craig and C. Neto, Langmuir **17**, 6018 (2001).
[35] J. M. Skotheim and L. Mahadevan, Physics of Fluids **17**, 092101 (2005).
[36] B. Saintyves, T. Jules, T. Salez, and L. Mahadevan, Proceedings of the National Academy of Sciences **113**, 5847 (2016).
[37] Y. Moroi, K. Motomura, and R. Matuura, Journal of Colloid and Interface Science **46**, 111 (1974).
[38] E. Fuguet, C. Ràfols, M. Rosés, and E. Bosch, Analytica Chimica Acta **548**, 95 (2005).
[39] K. Joshi and J. F. Gilchrist, Applied Physics Letters **116**, 083702 (2020).